

Ongoing chromosomal instability and karyotype evolution in human colorectal cancer organoids

Ana C. F. Bolhaqueiro^{1,8}, Bas Ponsioen^{2,8}, Bjorn Bakker³, Sjoerd J. Klaasen¹, Emre Kucukkose⁴, Richard H. van Jaarsveld¹, Judith Vivié¹, Ingrid Verlaan-Klink², Nizar Hami², Diana C. J. Spierings³, Nobuo Sasaki¹, Devanjali Dutta¹, Sylvia F. Boj⁵, Robert G. J. Vries⁵, Peter M. Lansdorp^{3,6}, Marc van de Wetering⁷, Alexander van Oudenaarden¹, Hans Clevers^{1,7}, Onno Kranenburg⁴, Floris Foijer³, Hugo J. G. Snippert^{2,9*} and Geert J. P. L. Kops^{1,9*}

Chromosome segregation errors cause aneuploidy and genomic heterogeneity, which are hallmarks of cancer in humans. A persistent high frequency of these errors (chromosomal instability (CIN)) is predicted to profoundly impact tumor evolution and therapy response. It is unknown, however, how prevalent CIN is in human tumors. Using three-dimensional live-cell imaging of patient-derived tumor organoids (tumor PDOs), we show that CIN is widespread in colorectal carcinomas regardless of background genetic alterations, including microsatellite instability. Cell-fate tracking showed that, although mitotic errors are frequently followed by cell death, some tumor PDOs are largely insensitive to mitotic errors. Single-cell karyotype sequencing confirmed heterogeneity of copy number alterations in tumor PDOs and showed that monoclonal lines evolved novel karyotypes over time in vitro. We conclude that ongoing CIN is common in colorectal cancer organoids, and propose that CIN levels and the tolerance for mitotic errors shape aneuploidy landscapes and karyotype heterogeneity.

Genomic instability is a hallmark of cancers in humans. It increases the probability of oncogenic events and creates a heterogeneous cell population with enhanced abilities to adapt and evolve^{1–3}. As a result, high intratumoral heterogeneity (ITH) causes incomplete response to therapy and an increased probability of relapse and is, therefore, associated with poor clinical outcome^{4–8}. Large-scale whole-genome-sequencing studies at the bulk and single-cell levels have revealed extensive regional differences in genetic mutations and gene copy numbers, which indicate a history of genomic instability^{6,9–20}. Such studies, however, have not been able to show whether genome instability is still ongoing in late-stage tumors and, if so, at what rate. Understanding the evolutionary dynamics of tumor genomes is clinically relevant since unstable genomic ITH is expected to have a different impact on tumor evolution and clinical response than stable genomic ITH²¹.

A prominent form of genomic instability is CIN, which is defined as an increased occurrence of chromosome segregation errors during cell divisions. CIN can cause whole-chromosome aneuploidies, which are found in the vast majority of human cancers^{22,23}, and has been implicated as a driver of chromosomal rearrangements^{24–27}. CIN is a dynamic cellular event that cannot be directly observed in living human tumors. It was first described as deviations of chromosome copy numbers (by FISH) in clonal populations of colorectal cancer (CRC) cell lines²⁸, and was inferred to exist at the adenoma stage, becoming more prominent in carcinomas^{29,30}. As human tumors are inaccessible for the study of CIN, monolayer cancer cell cultures

have been instrumental in acquiring insights into its prevalence and its causes. CIN has been directly observed by live-cell imaging in common monolayer cell lines from various cancer types, including breast cancer, colon cancer and glioblastoma^{31–34}. These studies have suggested various possible molecular causes for the CIN phenotype, which manifest as distinct types of segregation errors including multipolar spindles, anaphase laggards or chromatin bridges^{31,34–36}. However, owing to strong selection for ex vivo growth and subsequent decade-long in vitro evolution, it is unknown to what extent cell lines recapitulate the (diversity of) cellular traits of primary tumors³⁷. Moreover, disrupting tissue architecture has profound impacts on chromosome segregation fidelity³⁸, thus raising questions regarding the validity of using monolayer cell lines from carcinomas to infer mitotic tumor phenotypes. As such, it has remained unresolved whether human tumors experience ongoing CIN, whether there is clonal variability in CIN or whether there is a correlation between the extent of CIN and genomic ITH. Organoid culture technology^{39,40} offers an opportunity to address such questions. It provides the possibility of culturing tissues in three-dimensional cultures and without immortalization, while maintaining functional and phenotypic characteristics. Moreover, as pioneered for CRC, it enables establishment and analysis of 'living tumor biobanks' that encompass the clinical diversity of the disease^{41–47}. Organoids are amenable to live-cell microscopy, allowing the study of cellular dynamics and processes within the context of primary expanded cancer tissue from human patients with cancer^{48,49}. Here, we used

¹Oncode Institute, Hubrecht Institute-KNAW, University Medical Centre Utrecht, Utrecht, the Netherlands. ²Oncode Institute, Center for Molecular Medicine, University Medical Centre Utrecht, Utrecht, the Netherlands. ³European Research Institute for the Biology of Ageing, University of Groningen, University Medical Centre Groningen, Groningen, the Netherlands. ⁴Department of Surgical Oncology, UMC Utrecht Cancer Centre, University Medical Centre, Utrecht, the Netherlands. ⁵Foundation Hubrecht Organoid Technology (HUB), Utrecht, the Netherlands. ⁶Terry Fox Laboratory, BC Cancer Agency, Department of Medical Genetics, University of British Columbia, Vancouver, British Columbia, Canada. ⁷Oncode Institute, Princess Maxima Centre for Paediatric Oncology, Utrecht, the Netherlands. ⁸These authors contributed equally: Ana C. F. Bolhaqueiro, Bas Ponsioen. ⁹These authors jointly supervised this work: Hugo J. G. Snippert, Geert J. P. L. Kops. *e-mail: H.J.G.Snippert@umcutrecht.nl; g.kops@hubrecht.eu

various organoid biobanks to examine the occurrence, severity and nature of CIN in human CRC and to examine its relationship with karyotype ITH.

Results

Live-cell imaging of chromosome segregation errors in tumor PDOs. To examine chromosome segregation fidelity in CRC tissue, we made use of tumor PDOs obtained from 11 patients with CRC (Fig. 1a, Supplementary Fig. 1a). Such cultures retain the molecular CRC subtypes and closely recapitulate original tumor properties⁴¹. Out of the 13 tumor PDO lines, 8 were classified as hypermutated CRC PDOs (>10 mutations per megabase (Mb) of exomes)⁴¹, and of those 8 a further 6 also showed mismatch-repair deficiency, a hallmark of microsatellite instability (MSI) (Fig. 1c, Supplementary Fig. 1b). The remaining five PDOs (9T, 14T, 16T, 18T and 31T; where ‘T’ indicates tumor) were classified as non-hypermutated and contained mutations in genes that are frequently associated with CRC⁴¹ (Supplementary Fig. 1a). As controls, we analyzed colon PDOs that were obtained from healthy-looking tissue adjacent to the resected tumor of four patients (H1N, H2N, P1N1 and 26N; where ‘N’ indicates normal) (Fig. 1a).

Metaphase spreads showed that colon PDO H1N had a median chromosome number of 46 (Supplementary Fig. 2a), and bulk genome sequencing verified diploidy in two other normal lines (Supplementary Fig. 2b). Two tumor PDOs (14T and 19Tb) were near-diploid while all other tumor PDOs had median chromosome numbers between 50 and 72 (Supplementary Fig. 2a). Tumor PDO 19Ta contained two populations, one corresponding to tetraploid cells, which is indicative of polyploidization events in this organoid line. Polyploid ancestry was also likely for tumor PDO 24Tb (Supplementary Fig. 2a). For examination of chromosome segregation fidelity, organoids stably expressing H2B-Neon (to visualize chromatin) were imaged in three dimensions at 3–4-min intervals for 16–18 h. Mitotic events were classified as either correct or, in the case of obvious errors at the mid-anaphase stage, as incorrect (Fig. 1b and Supplementary Videos 1–4). Mean error rates in colon PDOs were low (1.5–6.1%, Fig. 1c). By contrast, all tumor PDOs showed elevated mean missegregation rates, ranging from approximately 10% and 12% in tumor PDOs 19Tb and U3T, respectively, to around 50% in tumor PDO 9T. Organoids in which the vast majority of divisions were erroneous were frequently observed in these populations. Of note, comparison of a colon PDO line with and without H2B-Neon expression, at early and late passage, showed that the experimental procedures had not affected CIN levels (Supplementary Fig. 3a) or karyotype⁵⁰ (Supplementary Fig. 3b). Each organoid line displayed various error types. Bulky anaphase chromatin bridges (chromatin stretches that span the two separating packs of chromosomes and that can subsequently undergo chromosomal breakage²⁴) were observed the most frequently (Fig. 1d). (Note that our live imaging approach cannot visualize ultra-fine anaphase bridges.) This is consistent with previous observations in monolayer cultures of CRC cell lines³¹ and in engineered human CRC organoids with artificially introduced cancer mutations⁴⁸. Tumor PDOs 7T, 14T and 19Tb had fewer anaphase bridges than other error types, possibly indicating that different causes predominantly underlie CIN in these lines.

MSI tumors are karyotypically heterogeneous. Unexpectedly, four of the six MSI⁺ tumor PDOs showed medium to high levels of CIN, as did the hypermutated 24Ta and 24Tb lines (Fig. 1c). The MSI cell line HCT116 has a polyploid subpopulation⁵¹, as do tumor PDOs 19Ta and 24Tb (Supplementary Fig. 2a). In contrast to current models^{52–55}, these data suggest that MSI and/or hypermutation and CIN phenotypes can co-exist. To further examine this, we performed single-cell karyotype sequencing (scKaryo-seq; see Methods) on frozen tissue of human MSI⁺ tumors (Fig. 2a).

This technique enables whole-genome sequencing at 0.01–0.1× coverage to quantify copy number alterations (CNAs) at >1-Mb resolution. We reasoned that if human MSI⁺ CRC tumors are indeed CIN, their cell populations should be heterogeneous for large CNAs. Analysis of CNAs in 24–50 single nuclei isolated from frozen MSI⁺ tumors showed that 3 out of 4 tumors had cells with gains and losses of whole chromosomes as well as of chromosomal segments (Fig. 2b). Importantly, substantial cell-to-cell variability in CNAs was observed, denoting karyotype heterogeneity and thus indicating likely missegregation events that were relatively recent. Combined with the observations from live imaging, these data indicate that MSI and CIN are not mutually exclusive. Karyotype complexities are predominantly observed in bulk sequencing of MSI⁻ cancers, which may be due to stronger selection for aneuploidies in these tumors.

CIN is a non-uniform phenotype in CRC PDOs. Colorectal cancers have a high degree of cell-to-cell heterogeneity^{10,15,56–58}, which is thought to shape the evolutionary dynamics of cell populations. We examined whether CIN is a uniform feature in a tumor cell population—that is, whether all cells in the tumor have a similar propensity to missegregate chromosomes during mitosis. While analyzing various independently created tumor PDO lines that express fluorescent H2B, we noticed differences between lines. For example, tumor PDO 9T line 2 showed lower median levels of CIN than other tumor PDO 9T-derived lines, and they displayed different copy numbers of chromosomes 4, 5 and 9 (Fig. 3a,b and Supplementary Fig. 4a,b). Tumor PDO19Ta-derived lines showed different ranges of observable CIN, and both tumor PDOs19Ta- and 14T-derived lines had different frequencies of mitotic error types (for example, tumor PDO 19Ta line 3 had very few multipolar divisions compared to tumor PDO 19Ta lines 1 or 2, and tumor PDO 14T line 1 showed predominantly lagging chromosomes, whereas tumor PDO 14T line 2 had mostly while anaphase bridges; Fig. 3c). These quantitative and qualitative variations in CIN raised the possibility that the parental line had intermixed subclones that became reduced after the infection and selection procedures.

Genome sequencing studies of various tumor types have shown that different subclones occupy spatially distinct regions of a tumor^{10,14,16}. The lines analyzed in Figs. 1 and 3 were polyclonal and established from a large population of cells from resected primary tumors⁴¹. To further examine non-uniformity of CIN, we made use of tumor PDOs that were derived from single cells from multiple regions of the same tumor. These tumor PDOs showed extensive diversity in mutational histories, transcriptome profiles and their response to drug treatments and as such reflect ITH⁵⁹ (Fig. 3d and Supplementary Fig. 4c). Three such sets—each of which was obtained from a different patient—were examined and one set (patient 1, P1) was classified as MSI (Supplementary Fig. 4d). All organoids showed CIN and anaphase bridges were the most frequently observed mitotic error in all samples (Fig. 3e–g and Supplementary Videos 5 and 6). Whereas all regional tumor PDOs of patient 1 and 2 displayed CIN to comparable degrees, those of patient 3 had substantially different median levels (comparison of regions A and B; Fig. 3f). One regional tumor PDO of patients 3 displayed significantly higher CIN than tumor PDOs from a neighboring region (53.7% versus 13%). We therefore conclude that CIN levels themselves can be subject to regional variation within a tumor PDO and as such may represent a component of intratumoral cellular heterogeneity.

Single-cell genome sequencing reveals karyotype heterogeneity in tumor PDOs. The organoid culture system offered a unique opportunity to directly test the hypothesis that ongoing CIN and a phenotype that is tolerant to aneuploidy contribute to cell-to-cell genomic heterogeneity^{21,60,61}. Having established that CIN is widespread in

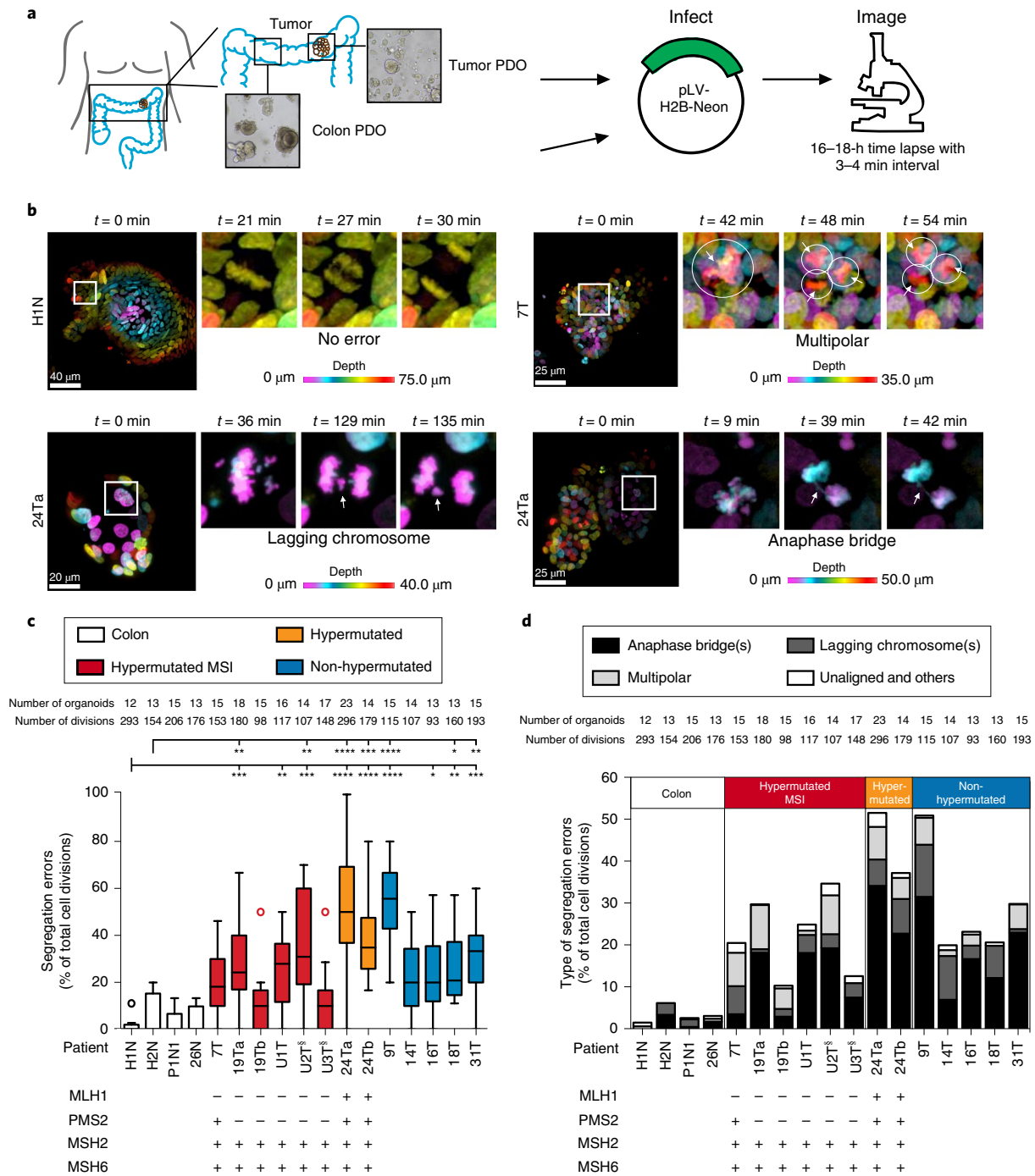


Fig. 1 | Live imaging of chromosome segregation errors in PDOs. **a**, Overview of sample derivation and imaging procedure. **b**, Representative stills of mitotic events in H2B-Neon-expressing PDOs. Chromosome segregation was imaged live at 3-min intervals for 16–18 h. H1N, healthy colon PDO; 7T and 24Ta, tumor PDOs. White arrows indicate mitotic errors. $n = 2$ or 3 independent experiments with similar results. See Supplementary Videos 1–4. **c**, Quantification of segregation errors per organoid observed in colon PDOs and tumor PDOs. Tumor PDOs were subdivided into hypermutated MSI (red), hypermutated (orange) or non-hypermutated (blue), depending on the frequency of mutations per Mb (>10 mutations per Mb versus <10 mutations per Mb, respectively, for hypermutated and non-hypermutated groups). Metastatic tumor PDOs are identified with \S . $n = 2$ or 3 independent experiments. $****P < 0.0001$, $***0.0002 < P < 0.0009$, $**0.0028 < P < 0.0096$, $*0.0277 < P < 0.0281$; non-parametric Kruskal-Wallis test. For all figures, data that are represented as box-and-whisker plots calculated using the Tukey method. For all box-and-whisker plots, the boxes represent quartiles 2 (Q2) and 3 (Q3); the horizontal line in the box represents the median; the whiskers represent the lowest values within $1.5\times$ the interquartile range of the lower quartile ($Q1 - 1.5\times(Q3 - Q1)$) and the highest values within $1.5\times$ the interquartile range of the upper quartile ($Q3 + 1.5\times(Q3 - Q1)$) and the circles indicate data points that are more than $1.5\times$ the interquartile range from the end of a box. **d**, Quantification of the types of segregation error, from the videos of 1C. Data are the mean percentage of segregation errors per organoid. Related to Supplementary Figs. 1–3.

our panel of tumor PDOs, we next determined the extent of variability in their karyotypes at the single-cell level using scKaryo-seq. Although bulk sequencing had revealed no aneuploidies in early

passages of two colon PDOs (see Supplementary Fig. 2b), scKaryo-seq showed that 26N had dominant aneuploidies in the regions of three chromosomes (Fig. 4a). Interestingly, sequencing of frozen

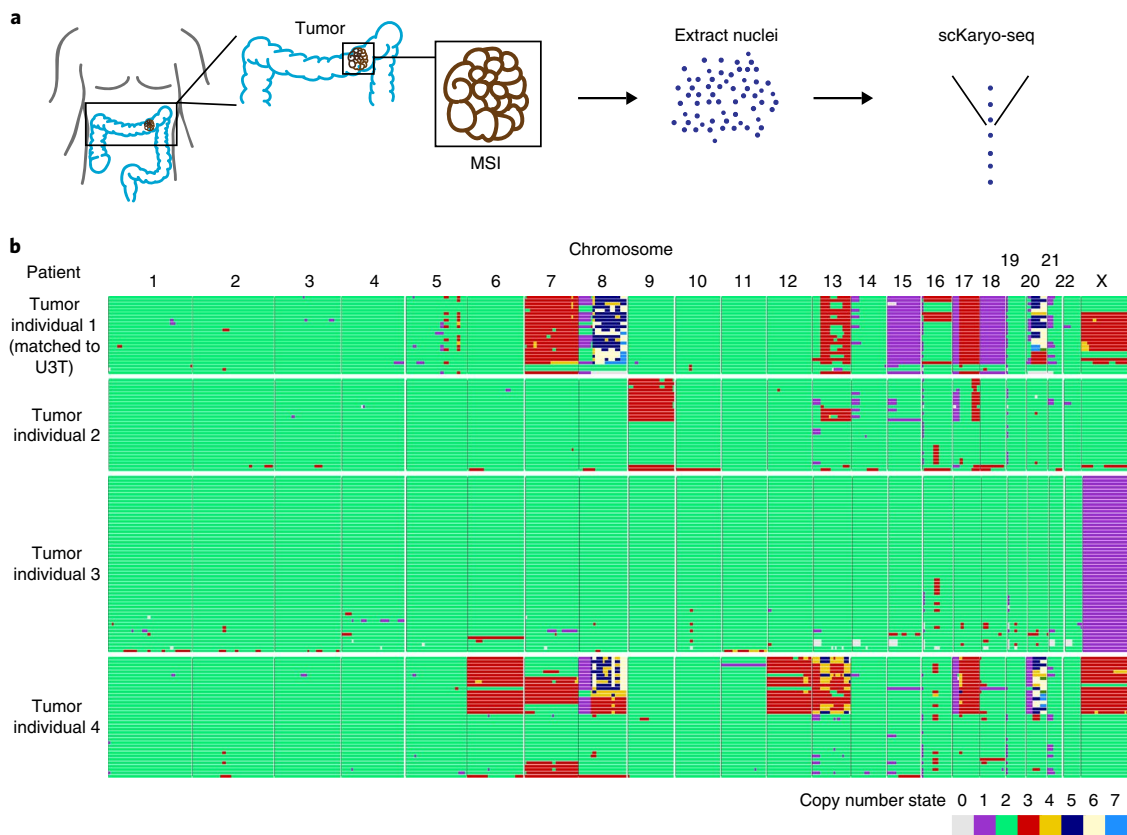


Fig. 2 | MSI tumors show karyotype heterogeneity. a, Overview of sample derivation and scKaryo-seq procedure. **b**, Genome-wide copy number plots of MSI tumors were generated using a modified version of the Aneupfinder algorithm. Each row represents a cell and the copy number state (in 5-Mb bins) is indicated in colors (with aberrations contrasting from green (2n)).

nuclei from healthy colon tissue of one individual revealed aneuploid cells (Supplementary Fig. 2c,d). Normal colon tissue can therefore have aneuploid cells and these may become dominant *in vitro*, either by drift or by selective pressures. Nevertheless, the cell population of colon PDO 26N was relatively homogeneous (Fig. 4a), consistent with the high mitotic fidelity that was observed by time-lapse imaging (Fig. 1c). By contrast, 10 out of 11 tumor PDO lines displayed substantial karyotype heterogeneity (Fig. 4a). The extent of karyotype heterogeneity tended to be higher in tumor PDOs with moderate to high CIN (Fig. 4b). We found no tumor PDOs that combined low karyotype heterogeneity with high CIN or vice versa. The correlation between the two features was nonetheless weak ($r^2=0.19$) and remained weak when heterogeneity was scored by assigning a copy number state to whole chromosomes (Supplementary Fig. 5e,f). Therefore, in all likelihood cellular features other than CIN itself additionally contribute to ITH. Nevertheless, in our limited set of samples, karyotype ITH is nearly always paired with moderate to high CIN.

Tolerance for mitotic errors varies between tumor PDOs.

Genomic ITH is the combined consequence of genomic instability and a tolerance phenotype that permits the survival and proliferation of daughter cells with altered karyotypes. We observed two- to threefold differences in proliferation rates and cell death frequencies at different time points after plating (Fig. 5a). For example, the p53-proficient tumor PDO 14T combined relatively slow growth with a relatively high fraction of dying cells in the population, whereas the reverse was true for tumor PDOs 9T and 16T. Similar CIN but different proliferation and death rates may be expected to result in different extents of genomic ITH.

To more directly monitor the consequences of segregation errors on cell viability, we monitored the fates of individual cells after correct or erroneous chromosome segregation events by long-term (~72 h) live imaging (Fig. 5b). Fates of individual daughter cells that could be tracked throughout the experiment were scored in three categories: (1) undergoing a subsequent cell division, (2) undergoing cell death or (3) neither death nor division (Fig. 5b,c and Supplementary Videos 7–9). We found that the percentage of cells that underwent a second division was generally higher when the previous cell division was correct (Fig. 5d). Notably, those characterized by segregation errors were substantially more often followed by cell death compared to correct mitotic divisions (Fig. 5d). Frequency of cell death appeared to be unrelated to the type of segregation error, with the possible exception of multipolar divisions (Supplementary Fig. 6a). However, the fates of 'sibling' daughter cells were often not identical (Supplementary Fig. 6b), suggesting that cell fates are influenced by asymmetric alterations in the genomes of the two daughter cells as a result of the segregation error.

Although death was a relatively frequent outcome following erroneous divisions, substantial differences in death rates could be observed between tumor PDOs (Fig. 5d). For example, death rates in tumor PDOs 24Ta and 24Tb were low regardless of whether the preceding division had mitotic errors. Moreover, proliferation in 24Tb continued at a very high frequency. Tolerance for CIN can therefore vary widely. Of note, owing to limitations in imaging, we were unable to ascertain whether non-dividing cells were permanently arrested (for example, senescent) or would eventually divide again or die. Interestingly, within the confines of our limited set, multiple-regression analysis suggested that aneuploidy level (and to a lesser extent, degree of heterogeneity) can be predicted from the degree of CIN combined with the

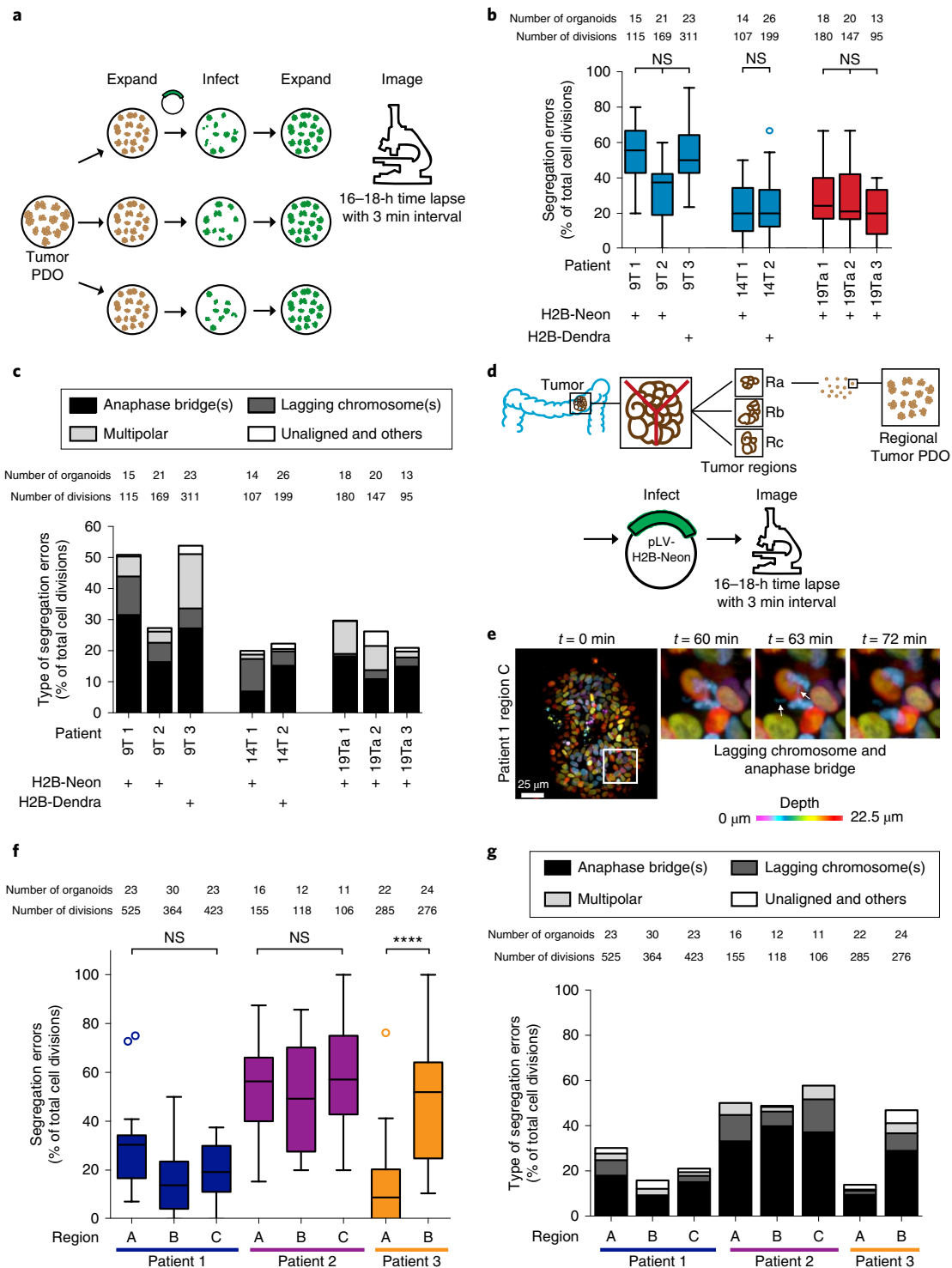


Fig. 3 | CIN is a non-uniform phenotype in CRC PDOs. **a**, Schematic of the parallel H2B-Neon infection method used to generate independent tumor PDOs and subsequent analysis using microscopy. **b**, Quantification of segregation errors per organoid observed in independently infected tumor PDOs and subsequent analysis using microscopy. **b**, Quantification of segregation errors per organoid observed in independently infected tumor PDOs. Tumor PDOs were subdivided into hypermutated MSI (red) or non-hypermutated (blue) depending on the frequency of mutations per Mb (>10 mutations per Mb versus <10 mutations per Mb, respectively). $n = 2$ or 3 independent experiments. A non-parametric Kruskal-Wallis test indicated $P > 0.05$. NS, not significant. **c**, Quantification of the types of segregation error, from the videos of 2B. Data are the mean percentage of segregation errors per organoid. **d**, Overview of the samples and imaging procedure to analyze regional tumor PDOs. **e**, Representative stills of Supplementary Video 6, visualizing mitotic events through the live imaging of H2B-Neon-expressing tumor PDOs (3-min intervals, 16–18 h). White arrows indicate the mitotic errors: one lagging chromosome and one anaphase bridge. $n = 2$ or 3 independent experiments with similar results. **f**, Quantification of segregation errors per organoid observed in two or three regional tumor PDOs from three different patients. $n = 2$ or 3 independent experiments. **** $P < 0.0001$; non-parametric Kruskal-Wallis test. **g**, Quantification of the types of segregation error, from the videos of 3F. Data are the mean percentage of segregation errors per organoid. Related to Supplementary Fig. 4c.

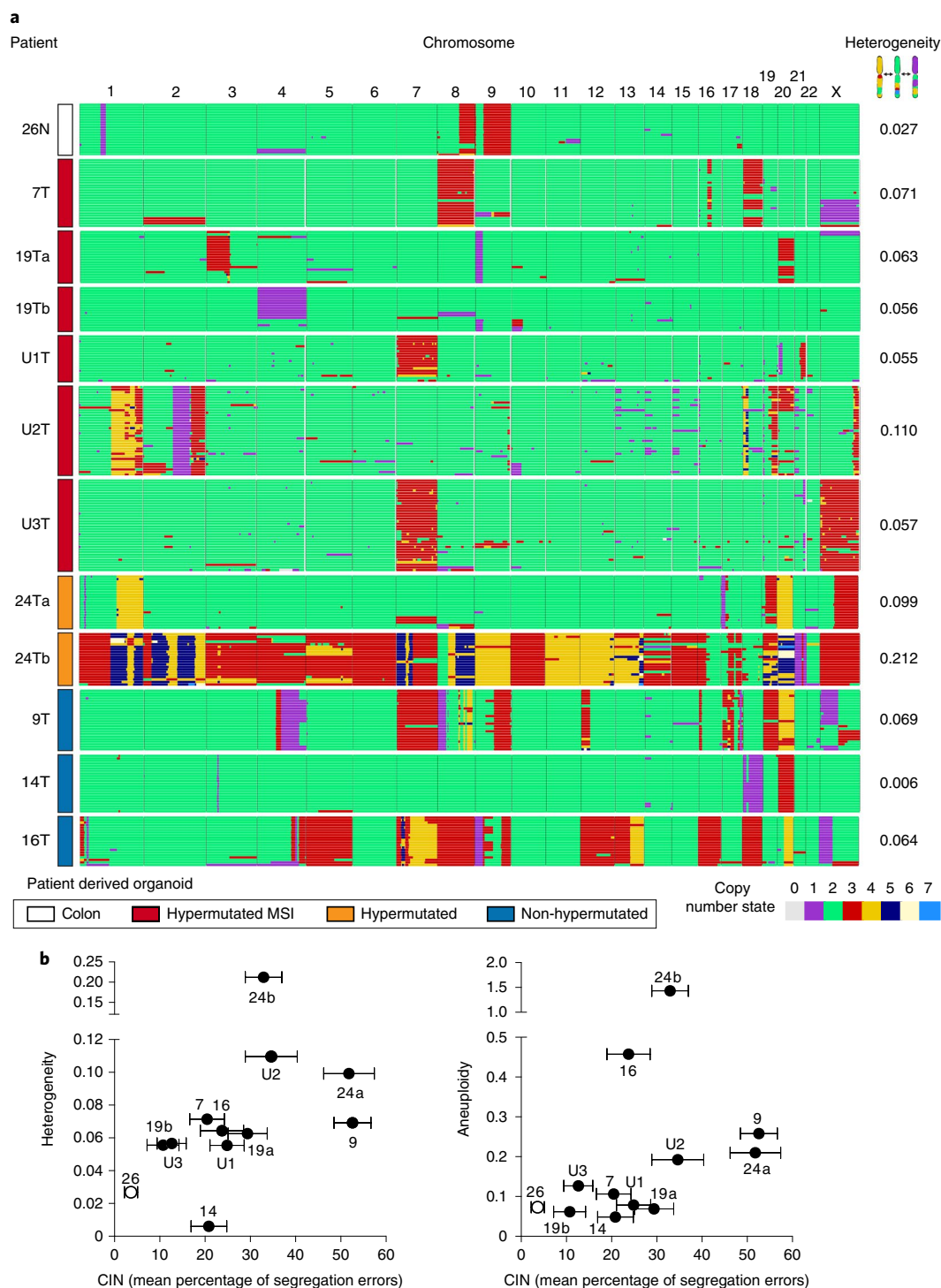


Fig. 4 | Single-cell genome sequencing reveals karyotype heterogeneity in tumor PDOs. a, Genome-wide copy number plots of colon PDOs and tumor PDOs were generated using a modified version of the Aneupfinder algorithm (left). Each row represents a cell and the copy number state is indicated in colors. Heterogeneity values per colon PDO and tumor PDO are shown (right). 7T, U1T, U2T and U3T are shown at 5-Mb resolution, the others at 2-Mb. **b**, Correlation plots of heterogeneity or aneuploidy versus CIN values (Pearson correlation). White circles, healthy colon PDOs; black symbols, tumor PDOs. Heterogeneity and aneuploidy scores obtained in 2- or 5-Mb bins. $n=1$ independent experiment. Mean CIN levels are derived from Fig. 1c. Data are mean \pm s.e.m. $n=2$ or 3 independent experiments. Related to Supplementary Fig. 5.

death ratio, growth rate or percentage of cells that continue dividing after an earlier erroneous mitosis (Fig. 5e,f and Supplementary Fig. 6c). Although other variables are likely to contribute, varying levels of CIN and tolerance to CIN seem important contributors to manifestation of aneuploidy and heterogeneity in a tumor PDO cell population.

In vitro karyotype evolution in tumor PDO 16T. Our data thus far suggested a contribution of CIN to karyotype heterogeneity. In agreement with this, the three regional tumor PDOs of patient 1 (see Fig. 3d,f) had unique aneuploidy profiles (Fig. 6a), indicating that karyotypically distinct subclones had evolved within the primary tumor.

To examine whether karyotype evolution can be observed in tumor PDOs, that is, whether subclones with novel karyotypes can appear over time, we generated three monoclonal tumor PDO 16T lines by seeding and clonal outgrowth of single cells (Fig. 6b). The three clones showed similar median CIN levels (Supplementary Fig. 7a) that were also comparable to the polyclonal founder line (see Fig. 1c). Furthermore, median CIN levels and error type frequencies were relatively stable over the 24-week period (Supplementary Fig. 7a,b). scKaryo-seq of the clones at week 3 after single-cell seeding showed that genomic CNAs had already diverged from that of the parental cells, and that karyotype heterogeneity was in line with that of the original tumor (Figs. 4a,6c and Supplementary Fig. 7c). Importantly, various novel karyotypes had appeared during 24 weeks of clonal organoid culturing. For example, chromosome 22 in 16T clone 2 was largely haploid at 3 weeks and regained diploidy of the q arm in nearly all cells at 24 weeks (Fig. 6c). Similarly, haploidy of chromosome 1 and tetrasomy of chromosome 18 appeared in clones 1 and 3, as did copy number increases in chromosomes 12 (clone 3) and 13 (clones 1 and 3). These data show that karyotypes evolve in vitro in tumor PDO 16T clones with chromosome instabilities.

Discussion

Tumor PDO models are currently the closest representatives of human tumors that are compatible with high temporal resolution analysis of cellular events. Tumor PDOs maintain histopathological features of native tumors, mutational and transcriptome profiles, and similarity between drug responses of tumor PDOs and patients in clinical trials^{41,44,45,49,62}. We now extend the use of these models to examine dynamic cell phenotypes. We show that CIN is widespread in colorectal carcinomas, that the severity of CIN can display subclonal and regional differences, and that CIN may facilitate karyotype evolution. Such analyses were not possible with the available CRC-derived monolayer cultures. Although the CIN events that were observed in the tumor PDOs may have various underlying causes, frequently observed error types were lagging chromosomes and, most frequently, anaphase chromatin bridges. The former are indicative of either a lack of chromosome spindle attachments or, more likely, erroneous attachments of the merotelic kind⁶³. Causes for bulky anaphase bridges include incomplete sister chromatid resolution, telomere fusions that have created dicentric chromosomes and incomplete replication. The latter has been reported to be a cause of anaphase bridges in CRC cell lines³¹. Interestingly, anaphase bridges were also the most prominent error observed in small intestine and colon organoids modified by CRISPR–Cas9 to model the intestinal adenoma-to-carcinoma transition⁴⁸.

Our analyses suggest that different degrees of error tolerance exist in tumor PDOs. p53 has been shown to limit proliferation of aneuploid cells, especially those in which a segregation error is accompanied by DNA damage^{64–66}. Very low proliferation rates and high

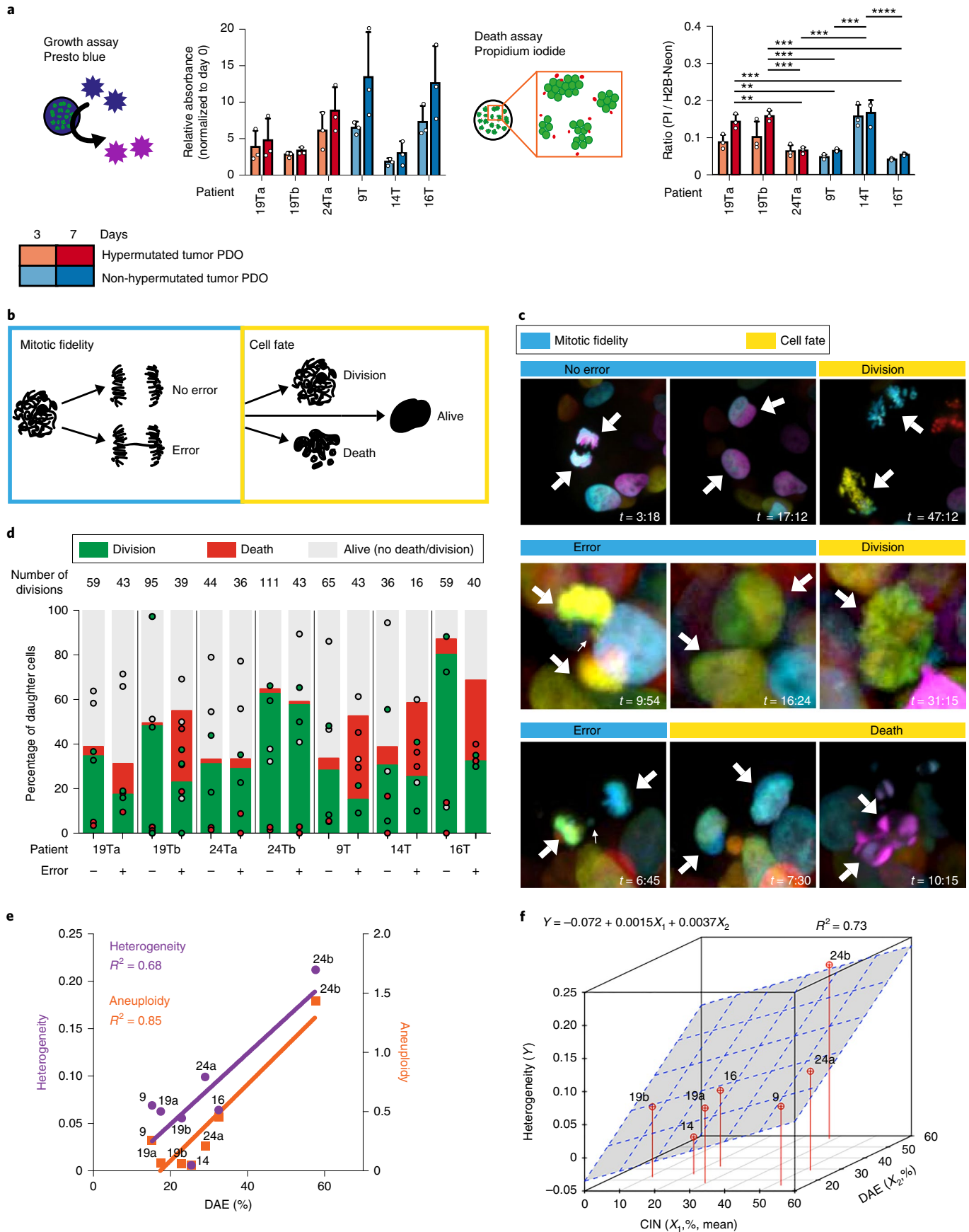
karyotype homogeneity despite medium to high CIN in p53-proficient tumor PDO 14T are consistent with this notion. Loss of *TP53* may thus simultaneously cause anaphase bridges and tolerance for these errors in the daughter cells. Nevertheless, tumor PDOs that had mutations in *TP53* were not universally tolerant for segregation errors (for example, tumor PDO 9T), suggesting that other factors in addition to p53 loss have a role in determining tolerance levels. Mutations in *BCL9L* have been reported to be associated with tolerance for aneuploidy in CRC samples⁶⁷, but these were found only in tumor PDO 19Tb (Supplementary Fig. 1a). The propensity for CIN and the intrinsic tolerance for changes in chromosomal copy numbers likely contribute to aneuploidy level and to degree of karyotype heterogeneity in patients, and even between different regional clones of a tumor. We here investigated only short-term viability after a mitotic error, but longer-term effects such as cell cycle arrest, senescence and cell death later than 3 d after the error are likely to contribute to viability scores. These differences may have profound effects on local karyotype evolution and thus on the birth of subclones with novel phenotypes. Of note, although in vitro karyotype evolution occurred in three PDO clones (Fig. 6), we have not directly shown that this results from CIN. It will be important in future efforts to quantify karyotype evolution in cultures with different CIN and CIN-tolerance levels, or in cultures in which these levels can be tuned.

Although we cannot exclude the possibility that culture procedures and the composition of the medium affect the phenotypes that we and others have observed, we demonstrate that human tumor organoids are a useful model to study dynamic cellular processes in human tumors, which has great potential to improve our understanding of tumor cell behavior. Our data show, for instance, that hypermutated MSI tumor PDOs can have substantial CIN. Multiple genomic instability phenotypes can thus co-exist and this may present new opportunities for therapeutic strategies. Moreover, we report the continuous presence of CIN in late-stage CRC tumor organoids, providing enhanced genomic plasticity compared to a heterogeneous but chromosomally stable population²¹. CIN, however, may also impose a vulnerability. Chromosomally unstable monolayer cultures succumb more readily to drugs that elevate the frequency of chromosome segregation errors⁶⁸. Biobanks of human tumor PDOs are a promising system for testing whether CIN levels correlate with observed (differential) sensitivities to such therapeutic agents in individual patients. Future efforts that combine CIN measurements with drug screening approaches on tumor PDOs may discover novel vulnerabilities in CIN tumors.

Online content

Any methods, additional references, Nature Research reporting summaries, source data, statements of data availability and associated accession codes are available at <https://doi.org/10.1038/s41588-019-0399-6>.

Fig. 5 | Tumor PDOs exhibit differential tolerance for mitotic errors. **a**, PDOs were plated for parallel assessment of growth rate (Presto blue; shown is absorbance relative to day 0) and death percentages (propidium iodide (PI) relative to H2B-Neon). $n = 3$ independent experiments. Data are mean \pm s.d. Data points from independent experiments are represented as dots. **** $P < 0.0001$, *** $0.0001 < P < 0.0006$, ** $0.0018 < P < 0.0020$ (one-way analysis of variance (ANOVA) with Tukey's multiple comparison test). **b**, Overview of the combined analysis of mitotic fidelity (correct or incorrect chromosome segregation) and subsequent fate of the daughter cells (cell division, death or neither of the two). **c**, Representative stills of live cell-fate tracking experiments of tumor PDOs. Analysis of mitotic fidelity (3-min intervals, 18 h) followed by cell-fate tracking (15-min intervals, 55–57 h). Time (t) is given in h:min. Large white arrows indicate the daughter cells, and small white arrows indicate mitotic errors. $n = 2$ or 3 independent experiments with similar results. See Supplementary Videos 7–9. **d**, Quantification of single-cell fate tracking experiments per tumor PDO. Mitotic events were classified as correct or erroneous. Data are the mean respective frequencies of subsequent cell division, subsequent death or the lack thereof. Data points from independent experiments are represented as dots. **e**, Correlation plots (simple regression) of heterogeneity (purple) or aneuploidy (orange) versus Division After Error (DAE). $n = 1$ (heterogeneity and aneuploidy) or 2 or 3 (DAE) independent experiments. Each dot represents a tumor PDO line. **f**, Correlation plot (multivariate linear regression) of heterogeneity versus CIN and DAE. Each dot represents a tumor PDO line and the surface plane represents the predicted values. Heterogeneity and aneuploidy scores that were obtained in 2-Mb bins were generated using a modified version of the Aneupfinder algorithm from Fig. 4. Mean CIN levels are derived from Fig. 1c. $n = 1$ (heterogeneity), 2 or 3 (DAE) or 2 or 3 (CIN) independent experiments. Related to Supplementary Fig. 6.



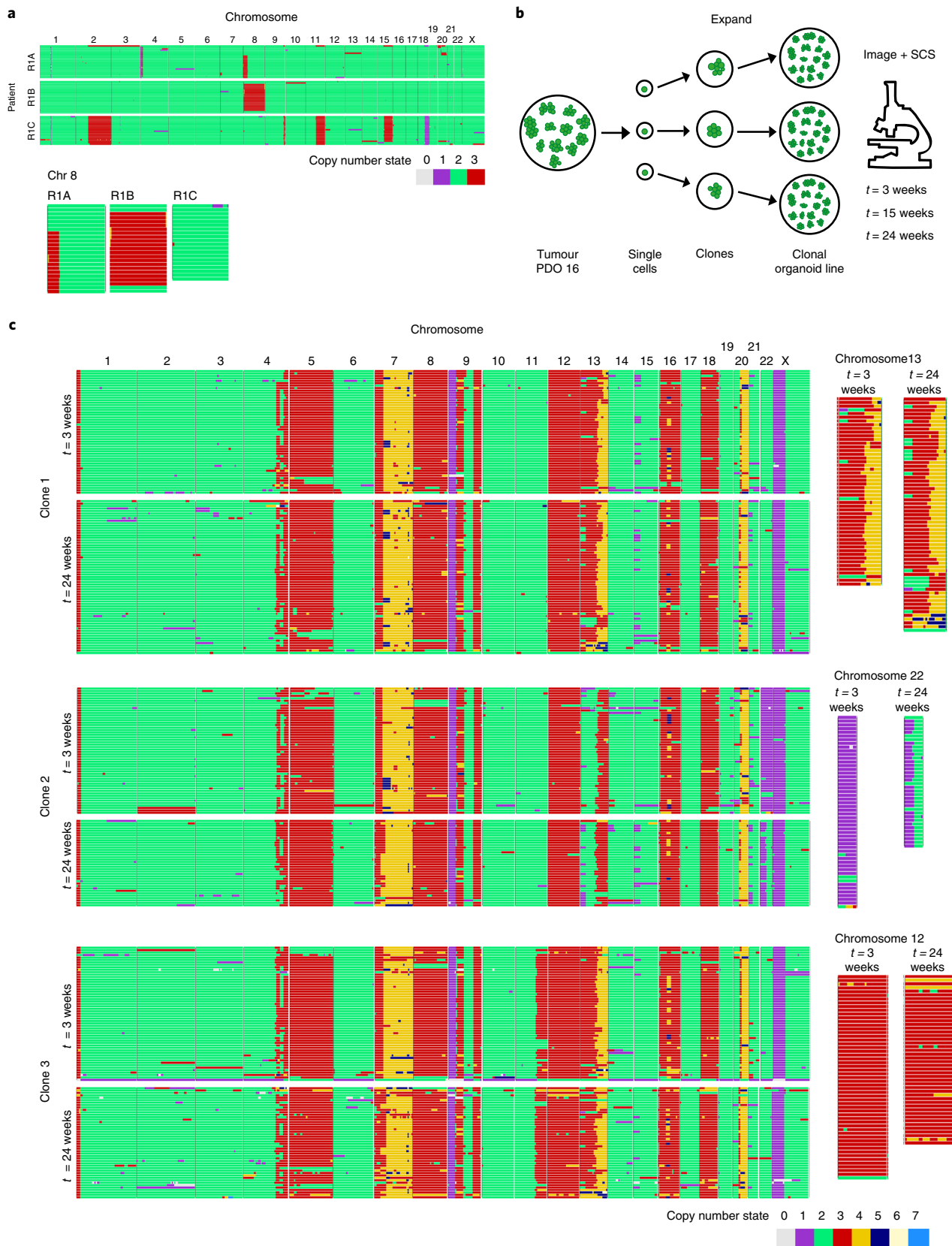


Fig. 6 | In vitro karyotype evolution of tumor PDO 16T. a, Genome-wide copy number plots of three regional tumor PDOs from patient 1 (Fig. 3). Each row represents a cell and the copy number state (2-Mb bins) is indicated in colors. Enlargement of chromosome 8 per regional tumor PDOs shows karyotypically distinct subclones. **b**, Schematic representation of the development and analysis of parallel monoclonal organoid lines derived from tumor PDO 16T. **c**, Left, genome-wide copy number plots of three clones derived from tumor PDO 16T at two time points (3 and 24 weeks after generation of the lines). Each row represents a cell and the copy number state (5-Mb bins) is indicated in colors. Enlargement of chromosome 13, 22 or 12 per clone shows karyotype evolution (right). Related to Supplementary Fig. 7.

Received: 16 May 2018; Accepted: 19 March 2019;
Published online: 29 April 2019

References

- Greaves, M. Evolutionary determinants of cancer. *Cancer Discov.* **5**, 806–821 (2015).
- Davis, A., Gao, R. & Navin, N. Tumor evolution: linear, branching, neutral or punctuated? *Biochim. Biophys. Acta Rev. Cancer* **1867**, 151–161 (2017).
- Swanton, C. Intratumor heterogeneity: evolution through space and time. *Cancer Res.* **72**, 4875–4882 (2012).
- Landau, D. A. et al. Mutations driving CLL and their evolution in progression and relapse. *Nature* **526**, 525–530 (2015).
- Andor, N. et al. Pan-cancer analysis of the extent and consequences of intratumor heterogeneity. *Nat. Med.* **22**, 105–113 (2016).
- Navin, N. E. Tumor evolution in response to chemotherapy: phenotype versus genotype. *Cell Rep.* **6**, 417–419 (2014).
- Gerlinger, M. & Swanton, C. How Darwinian models inform therapeutic failure initiated by clonal heterogeneity in cancer medicine. *Br. J. Cancer* **103**, 1139–1143 (2010).
- Kreso, A. et al. Variable clonal repopulation dynamics influence chemotherapy response in colorectal cancer. *Science* **339**, 543–548 (2013).
- Gerlinger, M. et al. Intratumor heterogeneity and branched evolution revealed by multiregion sequencing. *N. Engl. J. Med.* **366**, 883–892 (2012).
- Sottoriva, A. et al. A Big Bang model of human colorectal tumor growth. *Nat. Genet.* **47**, 209–216 (2015).
- Yates, L. R. et al. Subclonal diversification of primary breast cancer revealed by multiregion sequencing. *Nat. Med.* **21**, 751–759 (2015).
- Morrissy, A. S. et al. Divergent clonal selection dominates medulloblastoma at recurrence. *Nature* **529**, 351–357 (2016).
- Roynance, R. et al. Expression of regulators of mitotic fidelity are associated with intercellular heterogeneity and chromosomal instability in primary breast cancer. *Breast Cancer Res. Treat.* **148**, 221–229 (2014).
- Jamal-Hanjani, M. et al. Tracking the evolution of non-small-cell lung cancer. *N. Engl. J. Med.* **376**, 2109–2121 (2017).
- Kim, T. M. et al. Subclonal genomic architectures of primary and metastatic colorectal cancer based on intratumoral genetic heterogeneity. *Clin. Cancer Res.* **21**, 4461–4472 (2015).
- Gao, R. et al. Punctuated copy number evolution and clonal stasis in triple-negative breast cancer. *Nat. Genet.* **48**, 1119–1130 (2016).
- Morrissy, A. S. et al. Spatial heterogeneity in medulloblastoma. *Nat. Genet.* **49**, 780–788 (2017).
- Navin, N. E. Delineating cancer evolution with single-cell sequencing. *Sci. Transl. Med.* **7**, 296fs29 (2015).
- Navin, N. et al. Tumor evolution inferred by single-cell sequencing. *Nature* **472**, 90–94 (2011).
- Wang, Y. et al. Clonal evolution in breast cancer revealed by single nucleus genome sequencing. *Nature* **512**, 155–160 (2014).
- van Jaarsveld, R. H. & Kops, G. J. P. L. Difference makers: chromosomal instability versus aneuploidy in cancer. *Trends Cancer* **2**, 561–571 (2016).
- Duijif, P. H. G., Schultz, N. & Benezra, R. Cancer cells preferentially lose small chromosomes. *Int. J. Cancer* **132**, 2316–2326 (2013).
- Mitelman, F., Johansson, B. & Mertens, F. *Mitelman Database of Chromosome Aberrations and Gene Fusions in Cancer* (National Cancer Institute, 2018); <http://cgap.nci.nih.gov/Chromosomes/Mitelman>
- Janssen, A., van der Burg, M., Szuhai, K., Kops, G. J. P. L. & Medema, R. H. Chromosome segregation errors as a cause of DNA damage and structural chromosome aberrations. *Science* **333**, 1895–1898 (2011).
- Crasta, K. et al. DNA breaks and chromosome pulverization from errors in mitosis. *Nature* **482**, 53–58 (2013).
- Zhang, C.-Z. et al. Chromothripsis from DNA damage in micronuclei. *Nature* **522**, 179–184 (2015).
- Ly, P. et al. Selective Y centromere inactivation triggers chromosome shattering in micronuclei and repair by non-homologous end joining. *Nat. Cell Biol.* **19**, 68–75 (2017).
- Lengauer, C., Kinzler, K. W. & Vogelstein, B. Genetic instability in colorectal cancers. *Nature* **386**, 623–627 (1997).
- Shih, I. et al. Evidence that genetic instability occurs at an early stage of colorectal tumorigenesis. *Cancer Res.* **61**, 818–822 (2001).
- Cho, K. R. & Vogelstein, B. Genetic alterations in the adenoma–carcinoma sequence. *Cancer* **70**, 1727–1731 (1992).
- Burrell, R. A. et al. Replication stress links structural and numerical cancer chromosomal instability. *Nature* **494**, 492–496 (2013).
- Solomon, D. A. et al. Mutational inactivation of STAG2 causes aneuploidy in human cancer. *Science* **333**, 1039–1043 (2011).
- Thompson, S. L. & Compton, D. A. Examining the link between chromosomal instability and aneuploidy in human cells. *J. Cell Biol.* **180**, 665–672 (2008).
- Bakhom, S. F. et al. The mitotic origin of chromosomal instability. *Curr. Biol.* **24**, R148–R149 (2014).
- Thompson, S. L., Bakhom, S. F. & Compton, D. A. Mechanisms of chromosomal instability. *Curr. Biol.* **20**, R285–R295 (2010).
- Kops, G. J. P. L., Weaver, B. A. A. & Cleveland, D. W. On the road to cancer: aneuploidy and the mitotic checkpoint. *Nat. Rev. Cancer* **5**, 773–785 (2005).
- Sachs, N. & Clevers, H. Organoid cultures for the analysis of cancer phenotypes. *Curr. Opin. Genet. Dev.* **24**, 68–73 (2014).
- Knouse, K. A., Lopez, K. E., Bachofner, M. & Amon, A. Chromosome segregation fidelity in epithelia requires tissue architecture. *Cell* **175**, 200–211 (2018).
- Sato, T. et al. Single Lgr5 stem cells build crypt-villus structures in vitro without a mesenchymal niche. *Nature* **459**, 262–265 (2009).
- Sato, T. et al. Long-term expansion of epithelial organoids from human colon, adenoma, adenocarcinoma, and Barrett's epithelium. *Gastroenterology* **141**, 1762–1772 (2011).
- van de Wetering, M. et al. Prospective derivation of a living organoid biobank of colorectal cancer patients. *Cell* **161**, 933–945 (2015).
- Broutier, L. et al. Human primary liver cancer-derived organoid cultures for disease modeling and drug screening. *Nat. Med.* **23**, 1424–1435 (2017).
- Sachs, N. et al. A living biobank of breast cancer organoids captures disease heterogeneity. *Cell* **172**, 373–382 (2017).
- Fujii, M. et al. A colorectal tumor organoid library demonstrates progressive loss of niche factor requirements during tumorigenesis. *Cell Stem Cell* **18**, 827–838 (2016).
- Pauli, C. et al. Personalized in vitro and in vivo cancer models to guide precision medicine. *Cancer Discov.* **7**, 462–477 (2017).
- Schütte, M. et al. Molecular dissection of colorectal cancer in pre-clinical models identifies biomarkers predicting sensitivity to EGFR inhibitors. *Nat. Commun.* **8**, 14262 (2017).
- Zhang, M. et al. Aneuploid embryonic stem cells exhibit impaired differentiation and increased neoplastic potential. *EMBO J.* **35**, 2285–2300 (2016).
- Drost, J. et al. Sequential cancer mutations in cultured human intestinal stem cells. *Nature* **521**, 43–47 (2015).
- Verissimo, C. S. et al. Targeting mutant RAS in patient-derived colorectal cancer organoids by combinatorial drug screening. *eLife* **5**, e18489 (2016).
- Bakker, B. et al. Single-cell sequencing reveals karyotype heterogeneity in murine and human malignancies. *Genome Biol.* **17**, 115 (2016).
- Dewhurst, S. M. et al. Tolerance of whole-genome doubling propagates chromosomal instability and accelerates cancer genome evolution. *Cancer Discov.* **4**, 175–185 (2014).
- Buccitelli, C. et al. Pan-cancer analysis distinguishes transcriptional changes of aneuploidy from proliferation. *Genome Res.* **27**, 501–511 (2017).
- Taylor, A. M. et al. Genomic and functional approaches to understanding cancer aneuploidy. *Cancer Cell* **33**, 676–689 (2018).
- The Cancer Genome Atlas Network Comprehensive molecular characterization of human colon and rectal cancer. *Nature* **487**, 330–337 (2012).
- Lengauer, C., Kinzler, K. W. & Vogelstein, B. Genetic instabilities in human cancers. *Nature* **396**, 643–649 (1998).
- Lu, Y. W. et al. Colorectal cancer genetic heterogeneity delineated by multi-region sequencing. *PLoS ONE* **11**, e0152673 (2016).
- Losi, L., Baisse, B., Bouzourene, H. & Benhattar, J. Evolution of intratumoral genetic heterogeneity during colorectal cancer progression. *Carcinogenesis* **26**, 916–922 (2005).
- Mamlouk, S. et al. DNA copy number changes define spatial patterns of heterogeneity in colorectal cancer. *Nat. Commun.* **8**, 14093 (2017).
- Roerink, S. F. et al. Intra-tumour diversification in colorectal cancer at the single-cell level. *Nature* **556**, 457–462 (2018).
- Sansregret, L., Vanhaesebroeck, B. & Swanton, C. Determinants and clinical implications of chromosomal instability in cancer. *Nat. Rev. Clin. Oncol.* **15**, 139–150 (2018).
- Schukken, K. M. & Foijer, F. CIN and aneuploidy: different concepts, different consequences. *BioEssays* **40**, 1700147 (2018).
- Vlachogiannis, G. et al. Patient-derived organoids model treatment response of metastatic gastrointestinal cancers. *Science* **359**, 920–926 (2018).
- Gregan, J., Polakova, S., Zhang, L., Tolić-Norreylykke, I. M. & Cimini, D. Merotelic kinetochore attachment: causes and effects. *Trends Cell Biol.* **21**, 374–381 (2011).
- Santaguida, S. et al. Chromosome mis-segregation generates cell-cycle-arrested cells with complex karyotypes that are eliminated by the immune system. *Dev. Cell* **41**, 638–651 (2017).
- Soto, M. et al. p53 prohibits propagation of chromosome segregation errors that produce structural aneuploidies. *Cell Rep.* **19**, 2423–2431 (2017).
- Bakhom, S. F., Kabeche, L., Murnane, J. P., Zaki, B. I. & Compton, D. A. DNA-damage response during mitosis induces whole-chromosome missegregation. *Cancer Discov.* **4**, 1281–1289 (2014).

67. López-García, C. et al. BCL9L dysfunction impairs caspase-2 expression permitting aneuploidy tolerance in colorectal cancer. *Cancer Cell* **31**, 79–93 (2017).
68. Janssen, A., Kops, G. J. P. L. & Medema, R. H. Elevating the frequency of chromosome mis-segregation as a strategy to kill tumor cells. *Proc. Natl Acad. Sci. USA* **106**, 19108–19113 (2009).

Acknowledgements

We thank members of the Kops, Snippet and Clevers laboratories for reagents, suggestions and discussions; Y. Bollen and E. Stelloo for help with bulk genome sequencing; S. Sonneveld and F. Ferreira for help with R; and R. Wardenaar for the modifications on the Aneufinder algorithm. We are grateful to the Hubrecht Imaging Centre, particularly to A. Graaf, the Hubrecht Flow Cytometry facility, the USEQ Utrecht sequencing facility, and the ERIBA FACS and DNA sequencing facilities. This work is part of the Oncode Institute, which is partly financed by the Dutch Cancer Society, and was funded by the gravitation program CancerGenomiCs.nl from the Netherlands Organisation for Scientific Research (NWO), by a grant from the Dutch Cancer Society (KWF/HUBR-2015-7848), by a FP7-MSCA-ITN-2013 grant (PloidyNet, 607722), an NWO TOP grant (grant 91215003 to F.F.), an ERC starting grant (to H.J.G.S.) and by an Advanced Grant (to P.M.L.).

Author contributions

A.C.F.B., B.P., H.J.G.S. and G.J.P.L.K. conceived the project, designed experiments and wrote the manuscript. A.C.F.B., B.P., N.H., I.V.-K., R.H.v.J. and H.J.G.S. infected

and maintained the organoid lines. A.C.F.B., B.P. and H.J.G.S. performed live-cell imaging experiments, which were analyzed by A.C.F.B. E.K. performed the immunohistochemistry analyses. A.C.F.B. and B.P. performed all other organoid experiments. B.B., D.C.J.S. and S.J.K. performed single-cell sequencing, with help from P.M.L., F.F., J.V. and A.v.O. B.B. and S.J.K. are joint second authors. N.S., D.D., M.v.d.W. and H.C. provided all patient-derived tumor organoids. E.K., O.K., S.B. and R.G.J.V. provided frozen tissues.

Competing interests

H.C. is inventor on several patents related to organoid technology. All other authors declare no competing interests.

Additional information

Supplementary information is available for this paper at <https://doi.org/10.1038/s41588-019-0399-6>.

Reprints and permissions information is available at www.nature.com/reprints.

Correspondence and requests for materials should be addressed to H.J.G.S. or G.J.P.L.K.

Publisher's note: Springer Nature remains neutral with regard to jurisdictional claims in published maps and institutional affiliations.

© The Author(s), under exclusive licence to Springer Nature America, Inc. 2019

Methods

Human specimens. All human experiments were approved by the ethical committees of The Diaconessen Hospital Utrecht and University Medical Centre Utrecht (UMCU). Written informed consent from the donors for research use of tissue in this study was obtained prior to acquisition of the specimen. Samples were confirmed to be tumor or normal based on pathological assessment. Frozen tissue from MSI CRC tumors with identifiers HUB-02-B2-018 (tumor tissue from individual 2), HUB-02-B2-120 (tumor tissue from individual 4), HUB-02-B2-III-115 (tumor tissue from individual 3) and HUB-02-C2-098 (tumor tissue from individual 1, matched to organoid U3T) were provided by the Hubrecht Organoid Technology (HUB) foundation. Normal tissue from the UMCU biobank: C151N (colon tissue from individual 1).

Organoid culture. Derivation and maintenance of tumor PDOs and colon PDOs used in this study were described previously^{41,48,59}. We kept the nomenclature of the organoids obtained from the previous studies for P_xN and P_xT⁴¹ and regional tumor PDOs and P1N1 (ref. ⁵⁹). Organoids obtained from UMCU and the HUB foundation: HUB-02-C2-098 (U3T), CRM1 (U2T) and CRC29 (U1T). In summary, tumor PDOs were cultured in medium containing advanced DMEM/F12 medium (Invitrogen), HEPES buffer (Sigma-Aldrich, 1 mM), penicillin/streptomycin (Sigma-Aldrich, 1%), Ala-Glu (Sigma-Aldrich, 0.2 mM), R-spondin-conditioned medium (20%), Noggin-conditioned medium (10%), B27 (Thermo/Life Technologies, 1×), nicotinamide (Sigma-Aldrich, 10 mM), *N*-acetylcysteine (Sigma-Aldrich, 1.25 mM), A83-01 (Tocris, 500 nM), EGF (Invitrogen/Life Technologies, 50 ng ml⁻¹) and SB203580 (Invitrogen/Life Technologies, 3 μM). For colon PDOs, WNT-conditioned medium (50%, produced using stably transfected L cells) was added. For passaging, tumor PDOs were dissociated with TrypLE (Gibco) and colon PDOs were mechanically dissociated. The PDOs were replated in Matrigel in a pre-warmed 24-well plate. Rock inhibitor Y-27632 (Sigma-Aldrich, 10 μM) was added to culture medium upon plating for 2 d.

Immunohistochemistry. Tumor PDOs were cultured and grown for 10 d and collected with 10 mg ml⁻¹ dispase type II (Gibco) for 10–15 min. After washout of dispase type II with PBS (Sigma-Aldrich), the organoids were fixed in 4% formaldehyde solution at room temperature for 20 min. After centrifugation, the formaldehyde solution was aspirated, 200 μl 2% agar (Merck) solution was added and hardened on a pre-cooled dish. Subsequently, the agar droplets, which contained the tumor PDOs, were embedded in paraffin blocks. Immunohistochemistry of samples was performed on a BenchMark Ultra autostainer (Ventana Medical Systems). In brief, paraffin sections were cut with a thickness of 4 μm and deparaffinized in the instrument with EZ prep solution (Ventana Medical Systems) at 75 °C for 8 min. Heat-induced antigen retrieval was carried out using Cell Conditioning 1 (CC1, Ventana Medical Systems) for 32 min at 100 °C. For assessment of mismatch-repair status, immunohistochemistry was performed using the following antibodies: anti-human MLH1 (BD Pharmingen, clone G168-15, 1:20), anti-human PMS2 (Roche, clone EPR3947, ready-to-use), anti-human MSH2 (Roche, clone G219-1129, ready-to-use) and anti-human MSH6 (Abcam, clone EPR3945, 1:200). Slides were counterstained with hematoxylin and bluing reagent (Ventana Medical Systems).

Four-dimensional organoid imaging and image analysis. Organoids were transduced with a lentivirus containing an H2B-Neon-IRES-puromycin construct (pLV-H2B-Neon-ires-Puro)^{48,69}. After selection, these organoids were dissociated using TrypLE and plated in 15 μl Matrigel (Corning) or basement membrane extract (Amsbio) in a black glass-bottom 96-well plate (Corning). Three to four days later, the plate was mounted on a confocal laser-scanning microscope (Leica SP8X) or on a spinning-disk confocal microscope disk (Nikon/Andor CSU-W1 with Borealis illumination), equipped with atmospheric and temperature control. H2B-Neon-positive organoids were imaged in *xyzt* mode for 16–18 h at 37 °C at 3–4-min intervals using a ×40 water-immersion objective (NA 1.1 on the Leica SP8X and NA 1.15 on the Nikon SD). The Nikon SD was equipped with an additional ×1.5 lens in front of the CCD camera. For the Leica SP8X, we used 506 nm laser excitation from a tunable white-light laser, whereas for the Nikon SD we used a 3% 448 nm laser and 50 nm disk pinhole. In total, 14 to 23 *z*-sections at 2.5-μm intervals were imaged per organoid. Raw data were converted to videos using an ImageJ macro as described^{48,49}. Fidelity of all observed chromosome segregations was scored manually, guided by a custom-made ImageJ/Fiji macro for ordered data output.

For long-term fate-track imaging, organoids were filmed for 18 h at 3-min intervals to enable visualization of chromosome segregation fidelity, followed by 56 h at 15-min intervals to minimize phototoxicity. A drop of oil was placed on top of the medium to minimize evaporation of the medium. Any apoptotic event after 43 h was not considered to exclude potential effects of medium evaporation or phototoxicity.

Mitotic spreads. Organoids were treated with nocodazole (Sigma-Aldrich, 0.25 μg ml⁻¹) for 4 h and dissociated with TrypLE (Gibco) for 10–15 min. After washout of TrypLE with advanced DMEM/F12 medium (Invitrogen) containing HEPES buffer (Sigma-Aldrich, 1 mM), penicillin/streptomycin (Sigma-Aldrich,

1%), Ala-Glu (Sigma-Aldrich, 0.2 mM), cells were treated with KCl (0.56%) for 10 min at 37 °C. Subsequently, 200 μl of fixative solution (methanol:acetic acid; 3:1) was added while vortexing. After centrifugation, 1 ml fixative solution was added while vortexing and the cells were incubated at room temperature for 20 min. To visualize DNA, cells were stained with DAPI (Sigma-Aldrich, 1 μg ml⁻¹) for 5 min at room temperature. The cells were dropped on a slide using a 20-μl pipette and air-dried. Slides were incubated for 1 h at room temperature in PB3DT0.5, a solution that contains bovine serum albumin (Sigma-Aldrich, 3%), dimethylsulfoxide (Sigma-Aldrich, 1%) and Triton X-100 (Sigma-Aldrich, 10%) in PBS, followed by overnight incubation at 4 °C in PB3DT0.5 solution with CENP-C guinea pig primary antibody (MBL International SanBio, 1:1,000). After four 5-min washes with PB3DT0.5 solution, cells were incubated for 2–3 h at room temperature in PB3DT0.5 solution with goat anti-guinea pig 568 secondary antibody (Thermo/Life Technologies 1:600). The slides were washed four times with PB3DT0.5 solution, mounted in Prolong gold anti-fade (Thermo/Life Technologies) and analyzed on a DeltaVision Elite (×100 Super-Plan APO oil 1.4 NA objective).

Generation of clonal organoid lines. Organoids were treated with trypsin and single cells were deposited in single wells of a 96-well plate. Wells containing a single grown-out organoid after ~10 d were trypsinized and replated in basement membrane extract (Amsbio) for clonal expansion. Subsequently, the clonal lines were subdivided in parallel to maintain the culture, freeze for single-cell sequencing and perform *xyzt* time-lapse microscopy. With the culturing perpetuated, this cycle could be repeated several times, with intervals of 2–3 months.

scKaryo-seq. Organoids were dissociated into single cells with TrypLE (Gibco). After washout of TrypLE with advanced DMEM/F12 medium (Invitrogen) containing HEPES buffer (Sigma-Aldrich, 1 mM), penicillin/streptomycin (Sigma-Aldrich, 1%) and Ala-Glu (Sigma-Aldrich, 0.2 mM), cells were frozen in 500 μl of recovery cell culture freezing medium (Gibco), and further processed for sorting and sequencing (see below). Snap-frozen intact tissue was stained with 10 μg ml⁻¹ Hoechst 34580 (Sigma-Aldrich) and minced in a Petri dish, on ice, using a cross-hatching motion with two scalpels. The minced tissue was kept on ice for 1 h after which it was filtered through 70-μm and 35-μm strainers. Nuclei were sorted in a 384-well plate containing 5 μl mineral oil (Sigma-Aldrich) in each well and stored at –20 °C until further processing. Sequencing of samples from Figs. 2 and 4a (7T, U1-3T), and Supplementary Figs. 2c and 3b were performed as follows, all others were sequenced as described previously⁵⁰. Cell lysis was performed overnight at 50 °C using 0.05 units of Qiagen protease in 1× NEBuffer 4 (New England Biolabs) followed by heat inactivation at 75 °C for 20 min and 80 °C for 5 min. The genomic DNA was subsequently fragmented with 100 nl 1 U NlaIII (New England Biolabs) in 1× Cutsmart (New England Biolabs) for 60 min at 37 °C followed by heat inactivation at 80 °C for 20 min. Then, 100 nl of 1 μM barcoded double-stranded NlaIII adapters and 100 nl of 40 U T4 DNA ligase (New England Biolabs) in 1× T4 DNA ligase buffer (New England Biolabs) supplemented with 3 mM ATP (Invitrogen) was added to each well and ligated overnight at 16 °C. After ligation, samples were pooled and library preparation was performed as described previously⁷⁰. Libraries were sequenced on an Illumina Nextseq 500 with 1× 75-bp single-end sequencing. The fastq files were mapped to GRCH38 using the Burrows–Wheeler aligner. The mapped data were further analyzed using custom scripts in Python, which parsed for library barcodes, removed reads without a NlaIII sequence and removed PCR-duplicated reads. Copy number analysis was performed as described previously⁵⁰ with a modification as described in Supplementary Fig. 5a–d. The data are deposited in the ENA repository (accession number PRJEB27084).

Bulk whole-genome sequencing. Genomic DNA was isolated from bulk culture using the QIAamp DNA micro kit (Qiagen) and whole-genome amplified (Repli-g WGA kit, Qiagen). Amplified genomic DNA was sonicated and a library was prepared for 75-bp single-end sequencing (TruSeq Nano DNA Library Prep kit, Illumina). The data are deposited in the ENA repository (accession number PRJEB27084).

Presto blue cell viability assays. Organoids were plated in a 96-well plate in duplicate (15 μl per well). Reference viability values were determined by adding 90 μl of medium from tumor PDOs and 10 μl Presto blue solution (Invitrogen) to each well. This mix was also added to two empty wells for background correction. Organoids were incubated for 1 h at 37 °C after which absorbance was measured at 562 nm and at 620 nm. Cell viability was measured in a similar way at days 3, 7 and 10. The values were calculated as suggested by the product protocol: ((absorbance 562 nm tumor PDO – absorbance 620 nm tumor PDO) – (absorbance 562 nm empty well – absorbance 620 nm empty well))/((absorbance 562 nm tumor PDO day 0 – absorbance 620 nm tumor PDO day 0) – (absorbance 562 nm empty well day 0 – absorbance 620 nm empty well day 0)).

Apoptosis assays. Organoids were plated in three wells in a 96-well plate (10 μl per well). Apoptotic levels were evaluated by addition of propidium iodide, which intercalates with DNA fragments in apoptotic bodies and/or non-viable cells.

The ratio between propidium iodide-labeled DNA (red) and total DNA, as quantified by H2B-Neon positive signal (green) was calculated as described⁴⁹.

Statistical methods. We defined CIN as

$$\text{CIN} = \frac{1}{N} \sum_{n=1}^N \left(\frac{\text{number of erroneous divisions}}{\text{total divisions}} \times 100 \right)$$
 where N is the number of organoids. We included only organoids in which at least five cells divided during the video. For a set of N single cells with T bins, we define the aneuploidy score as $D = \frac{1}{TN} \sum_{n=1}^N \sum_{t=1}^T |c_{n,t} - e_t|$ where $c_{n,t}$ is the copy number state of cell n at bin t , and e_t is the euploid copy number at bin t (for example $e = 2$ for autosomes, and $e = 2$ or 1 for female and male X chromosomes, respectively). We define the heterogeneity score as $H = \frac{1}{TN} \sum_{n=1}^N \sum_{f=0}^S f m_{f,t}$ where $m_{f,t}$ is the number of cells with copy number s at bin t , and S is the total number of copy number states. $m_{f,t}$ is ordered for each bin such that $m_{f=0,t} \geq m_{f=1,t} \geq m_{f=2,t}$ and so on, in such a way that f is not necessarily equal to s . For Fig. 5f and Supplementary Fig. 6c, the data were fitted to a multivariate linear regression model: $Y = b + a_1 X_1 + a_2 X_2$ where X_1 is CIN, X_2 is the percentage of DAE, death as calculated as ratio of $\frac{\text{PI}}{\text{H2B}}$ or growth, and Y is heterogeneity score or aneuploidy score (see above). The P value evaluates the confidence with which the null hypothesis (that the variable has no correlation

with the dependent variables in a population) can be rejected, that is, it describes how well the dependent variables can describe the observed independent variable. The three-dimensional plot was generated using 3D Surface Plots (Plotly) in R.

Reporting Summary. Further information on research design is available in the Nature Research Reporting Summary linked to this article.

Data availability

The accession number for the single-cell and bulk whole-genome sequencing is [PRJEB27084](https://ena.ebi.ac.uk/ena/browser/view/PRJEB27084) (ENA repository).

References

69. Shaner, N. C. et al. A bright monomeric green fluorescent protein derived from *Branchiostoma lanceolatum*. *Nat. Methods* **10**, 407–409 (2013).
70. Muraro, M. J. et al. A single-cell transcriptome atlas of the human pancreas. *Cell Syst.* **3**, 385–394 (2016).

Reporting Summary

Nature Research wishes to improve the reproducibility of the work that we publish. This form provides structure for consistency and transparency in reporting. For further information on Nature Research policies, see [Authors & Referees](#) and the [Editorial Policy Checklist](#).

Statistical parameters

When statistical analyses are reported, confirm that the following items are present in the relevant location (e.g. figure legend, table legend, main text, or Methods section).

n/a Confirmed

- The exact sample size (n) for each experimental group/condition, given as a discrete number and unit of measurement
- An indication of whether measurements were taken from distinct samples or whether the same sample was measured repeatedly
- The statistical test(s) used AND whether they are one- or two-sided
Only common tests should be described solely by name; describe more complex techniques in the Methods section.
- A description of all covariates tested
- A description of any assumptions or corrections, such as tests of normality and adjustment for multiple comparisons
- A full description of the statistics including central tendency (e.g. means) or other basic estimates (e.g. regression coefficient) AND variation (e.g. standard deviation) or associated estimates of uncertainty (e.g. confidence intervals)
- For null hypothesis testing, the test statistic (e.g. F , t , r) with confidence intervals, effect sizes, degrees of freedom and P value noted
Give P values as exact values whenever suitable.
- For Bayesian analysis, information on the choice of priors and Markov chain Monte Carlo settings
- For hierarchical and complex designs, identification of the appropriate level for tests and full reporting of outcomes
- Estimates of effect sizes (e.g. Cohen's d , Pearson's r), indicating how they were calculated
- Clearly defined error bars
State explicitly what error bars represent (e.g. SD, SE, CI)

Our web collection on [statistics for biologists](#) may be useful.

Software and code

Policy information about [availability of computer code](#)

Data collection

Fluorescent images were collected using SoftWorx 6.0 software (Applied Precision/GE Healthcare), Nikon Imaging Software (NIS-Elements AR 5.51.00) and Leica Application Suite X (3.1.5.16308). Library preparation was performed using a Bravo Automated Liquid Handling Platform (Agilent Technologies, Santa Clara, CA, USA). Clusters for sequencing were generated on the cBot (Illumina). Single-end 50 bp sequencing was performed on an Illumina HiSeq 2500 at ERIBA (Illumina, San Diego, CA, USA).

Data analysis

Prism 6 was used for statistical analysis and graphical data presentation (<https://www.graphpad.com/>). ImageJ 1.49b Java 1.6.0_24 [64-bit] and ImageJ 1.49v Java 1.6.0_65 [64-bit] were used to analyze image data. We used three previously published custom made Fiji-macros (Verissimo et al., eLife, 2016): 1) to generate analyzable time-lapse movies from XYZT imaging data sets; 2) for detailed scoring of mitotic events in the time-lapse movies and 3) to quantify relative cell death rates in organoids over time, through surface determinations of Propidium Iodide. Raw sequencing data were demultiplexed based on library-specific barcodes and converted to fastq format using standard Illumina software (bcl2fastq version 1.8.4). The accession number for the single-cell whole genome sequencing of colorectal cancer organoids is PRJEB27084 (ENA repository). Analysis of single-cell sequencing data was performed with the AneuFinder pipeline (Bakker et al., Genome Biology, 2016), Python 2.7.5 and Burrows Wheeler Aligner 0.7.12. 3D plot was performed using R.

For manuscripts utilizing custom algorithms or software that are central to the research but not yet described in published literature, software must be made available to editors/reviewers upon request. We strongly encourage code deposition in a community repository (e.g. GitHub). See the Nature Research [guidelines for submitting code & software](#) for further information.

Data

Policy information about [availability of data](#)

All manuscripts must include a [data availability statement](#). This statement should provide the following information, where applicable:

- Accession codes, unique identifiers, or web links for publicly available datasets
- A list of figures that have associated raw data
- A description of any restrictions on data availability

The datasets generated during the current study are available from the corresponding author on reasonable request.

Field-specific reporting

Please select the best fit for your research. If you are not sure, read the appropriate sections before making your selection.

Life sciences Behavioural & social sciences Ecological, evolutionary & environmental sciences

For a reference copy of the document with all sections, see nature.com/authors/policies/ReportingSummary-flat.pdf

Life sciences study design

All studies must disclose on these points even when the disclosure is negative.

Sample size	No statistical method was used to predetermine the sample size. We have chosen a similar number of samples from each group of PDOs (colon, hypermutated and non-hypermutated). We aimed at having at least 3 PDOs from each group. Sample size and number of independent experiments are stated in the figure legend.
Data exclusions	No data is excluded if the experiments were successfully performed. We excluded PDOs which had less than five divisions per organoid.
Replication	All experiments were reliably reproduced. We performed each experiment at least twice. If the results were similar we assumed reproducibility of the experiments.
Randomization	All organoid pictures and movies were randomized.
Blinding	Region patient-derived tumor organoids movies were blinded analyzed.

Reporting for specific materials, systems and methods

Materials & experimental systems

n/a	Involvement in the study
<input type="checkbox"/>	<input checked="" type="checkbox"/> Unique biological materials
<input type="checkbox"/>	<input checked="" type="checkbox"/> Antibodies
<input checked="" type="checkbox"/>	<input type="checkbox"/> Eukaryotic cell lines
<input checked="" type="checkbox"/>	<input type="checkbox"/> Palaeontology
<input checked="" type="checkbox"/>	<input type="checkbox"/> Animals and other organisms
<input type="checkbox"/>	<input checked="" type="checkbox"/> Human research participants

Methods

n/a	Involvement in the study
<input checked="" type="checkbox"/>	<input type="checkbox"/> ChIP-seq
<input checked="" type="checkbox"/>	<input type="checkbox"/> Flow cytometry
<input checked="" type="checkbox"/>	<input type="checkbox"/> MRI-based neuroimaging

Unique biological materials

Policy information about [availability of materials](#)

Obtaining unique materials All unique materials are readily available from the authors or from the Foundation Hubrecht Organoid Technology (HUB), .

Antibodies

Antibodies used CENP-C guinea pig primary antibody (MBL International SanBio BV, 1:1000, PD030, Lot 005), anti-human MLH1 (BD Pharmingen, clone G168-15, Lot 7270524, 1:20), anti-human PMS2 (Roche, clone EPR3947, Lot V0001145, ready-to-use), anti-human MSH2 (Roche, clone G219-1129, Lot V0001056, ready-to-use), and anti-human MSH6 (Abcam, clone EPR3945, Lot GR262215-13, 1:200).

Validation

Validation is based on the datasheet from the manufacturer.

Human research participants

Policy information about [studies involving human research participants](#)

Population characteristics

Patients with tumors diagnosed as microsatellite unstable (MSI).

Recruitment

Participants were recruited only based on the MSI diagnosis.